JGR Biogeosciences

RESEARCH ARTICLE
10.1029/2022JG007055

Special Section:
The Earth in living color: spectroscopic and thermal imaging of the Earth: NASA's Decadal Survey Surface Biology and Geology Designated Observable

Wildfires Temperature Estimation by Complementary Use of Hyperspectral PRISMA and Thermal (ECOSTRESS & L8)

S. Amici[1], D. Spiller[2], L. Ansalone[3], and L. Miller[4]

[1]Istituto Nazionale di Geofisica e Vulcanologia, Rome, Italy, [2]School of Aerospace Engineering, Sapienza University of Rome, Rome, Italy, [3]Agenzia Spaziale Italiana, Rome, Italy, [4]Energy and Environment Directorate, Pacific Northwest National Laboratory, Richland, WA, USA

Abstract This paper deals with detection and temperature analysis and of wildfires using PRISMA imagery. Precursore IperSpettrale della Missione Applicativa (Hyperspectral Precursor of the Application Mission, PRISMA) is a new hyperspectral mission by ASI (Agenzia Spaziale Italiana, Italian Space Agency) launched in 2019. This mission provides hyperspectral images with a spectral range of 400–2,500 nm and an average spectral resolution less than 12 nm and a spatial resolution of 30 m/pixel. This study focuses on the wildfire temperature estimation over the Bootleg Fire, US 2021. The analysis starts by considering the Hyperspectral Fire Detection Index (HFDI) which is used to analyze the informative content of the images, along with the analysis of some specific visible, near-infrared and shortwave-infrared bands. This first analysis is used as input to perform a temperature estimation of the areas with active wildfire. Surface temperature is retrieved using PRISMA radiance and a linear mixing model based on two background components (vegetation and burn scar) and two active fire components. PRISMA temperatures are compared with LST (Land Surface Temperature) products from NASA's ECOSTRESS and Landsat 8 which imaged the Bootleg Fire before and after PRISMA. A critical discussion of the results obtained with PRISMA is presented, followed by the advantages and limitation of the proposed approach.

Plain Language Summary This work explores new opportunities for wildfire mapping and monitoring basing on recent technological achievements in the field of remote sensing and data analysis. The input data of this research study are provided by the new satellite PRISMA (*Precursore IperSpettrale della Missione Applicativa*, Hyperspectral Precursor of the Application Mission) from ASI (*Agenzia Spaziale Italiana*, Italian Space Agency). This spacecraft represents an innovative remote sensing mission for the observation of the Earth, as it provides images with a revolutionary quantity of spectral information which go far beyond the visible spectrum. Using PRISMA data, we study the Bootleg Fire during 2021 in the US, providing a descriptive analysis of the wildfire and a quantitative estimation of the temperatures achieved during the event. To confirm the results of our approach, we also compare the outcomes to the data provided by two other satellite missions: ECOSTRESS (ECOsystem Spaceborne Thermal Radiometer Experiment) and Landsat 8. Hence, a critical discussion of the results obtained with PRISMA is presented in order to report advantages and limitation of the proposed approach.

Key Points:

- Hyperspectral fire index for PRISMA data has been retrieved to create a wildfire detection map of Bootleg Fire, Oregon 2021
- Hot temperatures of wildfire has been estimated by applying linear mixture analysis to PRISMA data
- Multisensor approach has been used to characterize Bootleg wildfire temperature evolution

Correspondence to:
S. Amici,
stefania.amici@ingv.it

Citation:
Amici, S., Spiller, D., Ansalone, L., & Miller, L. (2022). Wildfires temperature estimation by complementary use of hyperspectral PRISMA and thermal (ECOSTRESS & L8). *Journal of Geophysical Research: Biogeosciences*, *127*, e2022JG007055. https://doi.org/10.1029/2022JG007055

Received 13 JUL 2022
Accepted 21 NOV 2022

Author Contributions:
Conceptualization: S. Amici
Formal analysis: S. Amici, D. Spiller
Methodology: S. Amici, D. Spiller
Resources: S. Amici
Software: D. Spiller
Supervision: L. Ansalone
Validation: S. Amici
Writing – original draft: S. Amici, D. Spiller, L. Miller
Writing – review & editing: L. Ansalone

1. Introduction

Wildfires are natural phenomenon which both influence and are influenced by climate change (Grutzen & Andreae, 1990). They have been operating for millions of years driving the plant evolution (Archibald et al., 2018; Pausas & Keeley, 2009) influencing the distribution of biomes and plant community, the O_2 contribution (Rogers et al., 2020) and remain necessary for the persistence of key terrestrial ecosystems on Earth (Pausas & Bond, 2019). However, the rapid change in fire regimes driven by extreme weather, land use change, vegetation distribution and climate change (Veraverbeke et al., 2017; Ward et al., 2012) result in more intense and frequent fires with increased sizes and altered seasonality and severity (Abatzoglou & Williams, 2016; McLauchlan et al., 2020; R. G. Miller et al., 2019) which affects negatively the ecosystem resilience, natural and cultural resources, infrastructure and harm human health (Ward et al., 2012).

A blend of factors as fire intensity, rate of spread, residence time, intensity, flame lengths and combustion phase (e.g., smoldering, flaming and associated temperature) characterize the way a fire reacts (fire behavior)

to the influences of fuel, weather and topography and can be linked with the ecological processes (McLauchlan et al., 2020).

Wildfire temperature retrieval (Kennard et al., 2005) is of great interest as it helps to characterize wildfires effects and their potential impact. For example, diverse temperatures of a fire are associated to diverse types of particles and gas emissions (Andreae, 2019; Andreae & Merlet, 2001; Boulet et al., 2011; Freeborn et al., 2008; Kohlenberg et al., 2018; Ross et al., 2013; Wooster et al., 2005) while studies have linked wildfires temperature to the degree of damage that fires cause to the landscape (severity) (Auld & O'Connell, 1991; Dickinson & Johnson, 2001).

In the last few decades Earth Observation (EO) satellite have been used to analyze many fire characteristics, including: fire intensity (Johnston et al., 2017) fire temperature (Barducci et al., 2004; Dennison & Matheson, 2011; Matheson & Dennison, 2012; Waigl et al., 2019), fire radiative power (FRP) (Kaufman, Justice, et al., 1998; Matson & Dozier, 1981; Wooster et al., 2005), smoke composition (Kaufman, Hobbs, et al., 1998; Ross et al., 2013; van Leeuwen & van der Werf, 2011) and vegetation mortality (Bright et al., 2019; Key & Benson, 2006; J. D. Miller & Thode, 2007; Quintano et al., 2015; Roy et al., 2006; Zheng et al., 2016).

Detection and accurate monitoring of risk areas is becoming increasingly important to counteract severe and destructive wildfires. As reported in the survey paper (Barmpoutis et al., 2020), satellite-based optical remote sensing (RS) represents a cost-effective way to detect, map, and investigate wildfires. For instance, in Domenikiotis et al. (2002, 2003) the assessment of the burned areas was investigated using the National Oceanic and Atmospheric Administration/Advanced Very High-Resolution Radiometer (NOAA/AVHRR) and Landsat (Chuvieco et al., 2019; Roy et al., 2019). Active fire localization from space traditionally makes use of sensors operating in the Middle Infrared (MIR) between 3 and 5 μm and Thermal Infrared (TIR) between (8–12 μm) as these two are not influenced (Kaufman et al., 1990) by reflectance component. For example, NASA is providing near real-time global fire "hotspot" monitoring using MIR and TIR data from MODIS and VIIRS (Davies et al., 2020). The detection algorithms are based on the strong contrast between emission spectra of ambient not burning areas and areas of active fires (flaming temperature 1000 K and smoldering 600 K), with the availability of MIR and TIR bands enabling the development of subpixel fire detection (Wooster et al., 2013). However, because of the emitted spectral radiance in the MIR (3–5 μm) atmospheric window is about three order of magnitude higher that the ambient land surface, sensors need to implement specific strategy to minimize saturation effect. For example, MODIS has two bands centered 3.96 μm with different saturation temperature and the Land Surface Temperature Radiometer (SLSTR) on board of Sentinel 3 has two bands, F1 (3.74 μm) and F2 (10.85 μm) optimized for fire detection.

In this study we focus on active fires and techniques to retrieve temperatures by using the SWIR (Short Wavelength InfraRed) spectral range. The use of SWIR spectral channels to detect wildfire has been researched by Morisette et al. (2007) who developed a detection algorithm based on the bands 8 centered at 2,330 nm and band 3 centered at 820 nm available in the Advanced Spaceborne Thermal Emission and Reflection Radiometer (ASTER) sensor on board of Terra satellite; the algorithm was later applied to different ecosystems (Csiszar et al., 2006; Giglio et al., 2008; Morisette et al., 2007) with promising results.

Hyperspectral sensors mounted on airborne platforms such as NASA's AVIRIS have been used to derive daytime hyperspectral fire detection indices (Dennison, 2006; Dennison & Roberts, 2009; Vodacek et al., 2002). Still, two aspects in fire detection with hyperspectral technology need to be emphasized: (a) the detection of the emitted radiance must be separated from the reflected surface reflectance, (b) if the fire occupies a small percentage of the pixel, the result is a dilution effect of the measured strength of the radiance which can be difficult to separate from the background. Later, other airborne sensors such as the SIMGA (Amici et al., 2011) have been used to test wildfires detection indexes on Mediterranean ecosystems. Temperature retrieval by using hyperspectral sensors have been initially investigated by Green et al. (1998) and Dennison and Roberts (2009) by using AVIRIS (Boardman & Green, 2000).

There have been few evaluations for the utility of hyperspectral (HS) data from satellite platforms, mostly limited by the availability of such sensors. Previous results based on NASA's EO-1 Hyperion have shown the HS potentialities for remote sensing applications (Waigl et al., 2019) for both fire detection and temperature retrieval over selected Alaskan boreal forest fires. Hyperspectral indices for fire detection and monitoring include

the continuum-interpolated band ratio (CIBR) that measures the depth of a carbon dioxide absorption line at 2,010 nm, the potassium emission, and the Hyperspectral Fire Detection Index (HFDI).

The problem of temperature estimation using HS data has been covered in previous research, such as Barducci et al. (2004), Dennison (2006), Dennison and Matheson (2011), Matheson and Dennison (2012). The wildfire temperature parameter is relevant to characterize wildfires and their potential impact on both natural and anthropic environments. Different temperatures of a fire are associated with diverse types of particles and gas emissions. The temperature of the fire is also vital to deriving the radiative power (FRP) which describes the rate of emitted thermal energy (Kaufman, Justice, et al., 1998; Matson & Dozier, 1981; Wooster et al., 2005).

In this paper, HS data from the Italian satellite PRISMA (PRecursore IperSpettrale della Missione Applicativa) will be used previous studies already focused on PRISMA for different land applications. For instance, PRISMA data have been used to perform a preliminary crop type mapping analysis, specifically a simple one-dimensional convolutional neural network has been proposed to solve a binary classification problem (Spiller, Ansalone, Carotenuto, & Mathieu, 2021). Moreover, wildfires in Australia have been studied using the same convolutional neural network as the previous study to carry out a multi-class semantic segmentation, and providing a preliminary temperature estimation analysis (Spiller, Ansalone, Amici, et al., 2021).

The area of interest of this study is located in Oregon (USA) over a large and rapidly expanding fire during July 2021. Overall, fire activity in the US was similar to both the 5 and 10 year averages, though compared to the last 10 years, some areas such as the Pacific Northwest experienced higher number of wildfires (+61%) and other areas such as Alaska were lower (−24%), as well as very different areas burned (Pacific Northwest +40%, Alaska −78%) (National Interagency Coordination Center, 2022).

The continuous spectral signature of PRISMA along with neural network analysis can open new unexplored research opportunities (Amici et al., 2011; Piscini & Amici, 2015). The main contributions of this work to the state-of-the-art are the following:

1. Qualitative and quantitative analysis of the area of interest using PRISMA data and the HFDI index.
2. Development of the algorithm for temperature retrieval, improving and adapting to PRISMA an existing approach discussed in literature (Waigl et al., 2019).
3. Comparison of the obtained results with ECOSTRESS and LANDSAT 8 data.

The rest of the paper is organized as follows. Section 2 deals with the description of the satellite-based data used for this work. The methodologies are described in Section 3. The results of the proposed analyses are reported in Section 4, followed by a critical discussion of the outputs in Section 5. Finally, conclusions are provided in Section 6.

2. Data

In this section, the region of interest and the data used for this study are discussed. It is noteworthy that the choice of the study area is dictated by the opportunity of having good temporal overlap of different sensor data over the Bootleg Fire to perform a comparison analysis. Additionally, the hyperspectral data approach proposed in this study could be extended to other areas and applications.

2.1. Study Area

The Bootleg Fire started on 6 July 2021 in the Fremont-Winema National Forest in Oregon (approx. 42.616°N, −121.421°E), with the cause attributed to lightning. It gained immediate and widespread attention in the U.S. for two reasons. First, the Bootleg Fire was co-located with a high-voltage transmission line connecting hydropower from the Pacific Northwest to electricity demand centers in Los Angeles, California. Second, the fire's area expanded incredibly fast (Figure 1). The fire area was a mix of grass/shrub and open to dense timber stands, which previously experienced beetle kill, resulting in concentrations of dry forest fuels. On July 15, airborne data collections were not possible because the Bootleg Fire was generating pyrocumulus clouds and its own weather along its southeast extent. Nine days later, at the time of the satellite acquisitions on 17 July 2021, the Bootleg Fire was about 274,000 acres (1,008 km^2) (National Interagency Coordination Center, 2022), and would not be fully contained until 1 October 2021 with a final extent of 413,717 acres (1,674 km^2).

Figure 1. Bootleg fire, northeast flank. From INCIWEB—Incident Information System—https://inciweb.nwcg.gov/incident/photograph/7609/38/119119.

2.2. Remote Sensing Satellite Data

In this section the data used for the analysis of wildfires in the areas of interest is described. Even though the focus of this research is on the hyperspectral data from PRISMA, ECOSTRESS and Landsat 8 data were also used to verify the results and add consistency to our PRISMA findings. The overall features of the three sensors are reported in Table 1.

2.2.1. PRISMA

PRISMA is the Italian hyperspectral mission launched on 27 March 2019 on board the VEGA (Vettore Europeo di Generazione Avanzata) rocket by ASI (Italian Space Agency). PRISMA represents the first mission with a dedicated hyperspectral (HS) camera, though other similar missions have been recently launched (Guanter et al., 2015) or are planned in the future years (Carmona et al., 2017; Cawse-Nicholson et al., 2021; Nieke & Rast, 2018).

The PRISMA sensor is a pushbroom instrument with a 30 km wide imaging swath composed by two cameras: the optical spectrometer (hyperspectral camera) operates in the spectral range spanning between 400 and 2,500 nm with a spectral resolution ≤12 nm and at Ground Sampling Distance (GSD) of 30 m/pixel and a Panchromatic camera that acquires the same area at 5 m/pixel. PRISMA characteristics are listed in Table 1 (PRISMA User Manual - Issue 1.2, 2020) while extended description of instrument performances and characteristics can be found in Ananasso et al. (2009), Candela et al. (2016), Coppo et al. (2020), Galeazzi et al. (2008), Guarini et al. (2018), Loizzo et al. (2016, 2018, 2019).

PRISMA is quite unique as it offers a free of cost on demand acquisition request system based on a priority list. This public request system was used to place a strip map over the likely Bootleg Fire's future extent. The PRISMA data are released in four levels:

1. Level 1 (Hyperspectral/PAN) is radiometrically corrected and calibrated TOA (Top Of Atmosphere). In the specific the L1 TOA data have been used for the Hyperspectral Fire Detection Index.
2. Level 2B Geolocated at Ground Spectral Radiance Product (Hyperspectral/PAN);
3. Level 2C Geolocated at-surface Reflectance Product (Hyperspectral/PAN);
4. Level 2D Geocoded version of the Level 2C product (Hyperspectral/PAN) [MicrosoftWord-PRISMAUserManual_Is1_1.docx(asi.it)].

Table 1
PRISMA, ECOSTRESS and Landsat 8 Sensors Characteristics

Feature	PRISMA	ECOSTRESS	Landsat 8	Unit
Swath width	30	384 (at 400 km)	185	km
Spatial resolution	30 (VIS-SWIR) 5 (PAN)	70	30 (VIS-SWIR) 100 (TIR) 15 (PAN)	m
Spectral channels	VNIR 66 channels, (0.4–1.010) SWIR (174 channels 0.920–2.5) PAN 1 channel (400–700)	SWIR 1 (1.66 not measured) TIR 5 channels (8.29, 8.78, 9.20, 10.49–12.09)[a]	VIS 5 channels (0.433–0.885) SWIR 3 channels (1.560–2.2) TIR 2 channels (10.9,12.0)	μm
Spectral bandwidth	VNIR (0.009–0.013) SWIR (0.009–0.0145)	TIR (0.35, 0.31, 0.39, 0.41, 0.61)	N/A	μm
Altitude	615	~400	705	km
Revisit time	29 days (nadir) and 7 days (off nadir)	4-5, daily over Contiguous US	16	Day
Radiometric accuracy	Better than 5%, (absolute)	Nominal 0.5 K	Nominal 0.4 K at 300 K (for the thermal channels only)	

[a]Only bands 8.29, 10.49 and 12.09 μm are currently being collected (https://ecostress.jpl.nasa.gov/instrument).

Table 2
Satellite Scenes Features

Sensor	Scene start time (UTC)	Scene	Latitude (N)	Longitude (W)
ECOSTRESS	17-07-2021 10:23:31	ECO2LSTE.001_SDS_LST_doy2021198102331_aid0001	42° 37' 16"	−121° 13' 24"
PRISMA	17-07-2021 19:03:31	PRS_L2B_STD_OFFL_20210717190331_20210717190335_0001[a]	42° 53' 18.96"	−121° 5' 2.4"
	17-07-2021 19:03:35	PRS_L2B_STD_OFFL_20210717190335_20210717190340_0001[b]	42° 37' 35.04"	−121° 10' 8.4"
Landsat 8	18-07-2021 18:50:00	LC08_CU_003005_20210718_20210802_02_ST	42° 54' 14"	−121 29' 24"

[a]Referred as PRISMA North image. [b]Referred as PRISMA South image.

In this study we are using the L2B Bottom of Atmosphere level data to derive the surface temperature.

2.2.2. Other Satellite Data: ECOSTRESS and LANDSAT 8

ECOSTRESS is a multispectral thermal camera Prototype HyspIRI Thermal Infrared Radiometer (PHyTIR) launched on July 2018 and operated from the International Space Station (ISS) from the Japanese Experiment Module-External Facility (JEM-EF). ECOSTRESS initially had 5 TIR channels, though some on-board memory failure early on resulted in 3 channels being operational after 15 May 2019 (Band 2: 8.78 μm, Band 4: 10.49 μm, and Band 5: 12.09 μm). We found that the closest coincident PRISMA and ECOSTRESS acquisitions over the Bootleg fire was 17 July 2021 at 10:23 UTC corresponding to 3:23 local US Pacific Time, about 9 hr in advance of PRISMA. ECOSTRESS data was accessed through the NASA AppEEARS system (LP DAAC - AppEEARS, 2022). The land surface temperature (LST) is usually available from the AppEEARS system in 1–2 days after acquisition and uses the method of Hook and Hulley (2019). This LST product is released at 70 × 70 m spatial resolution and as a digital number. A multiplicative correction factor equal to 0.02 transforms the digital number values into Kelvin (K).

Landsat 8 was launched on 11 February 2013. Landsat-8's Operational Land Imager (OLI) is a pushbroom sensor that operates in the visible (VNIR) and short-wave infrared (SWIR) spectral regions, and a TIRS sensor with two TIR bands. The Landsat temperature product is part of the Landsat Collection 2 U.S. Analysis Ready Data (ARD). It is calculated by applying the Single Channel algorithm on TIRS Band 10, and TM/ETM plus Band 6 (Zanter, 2018). The Provisional Land Surface Temperature based on Landsat 4–8 mission's product is available within the boundary of the North American Regional Reanalysis (NARR) grid and is accessible through Earth-Explorer USGS website (EarthExplorer, n.d.). The surface temperature (ST) values can be converted into Kelvin degrees by using the conversion formula

$$\mathrm{ST}(K) = \mathrm{ST}_{\mathrm{product}} \times 0.00341802 + 149 \quad (1)$$

as reported in Engebretson (2022).

2.2.3. Satellites Data Set

The programmed acquisition of PRISMA resulted in a PRISMA passage over the Bootleg Fire on 17 July 2021 at 19:03 UTC (Table 2) corresponding to 12:03 p.m. local time. Due to the spatial extent of the fire, the mosaicking of two PRISMA images was implemented to cover the area of the fire (Figure 2). The false color composition is used to highlight unburned vegetation in red, burnt areas in black-brown and smoke released by active fires in blues.

The closest to the PRISMA acquisition were ECOSTRESS on 17-07-2021 at 10:23 UTC corresponding to 3:23 a.m. local time and Landsat 8 on 18-07-2021 (Table 2) at 18:50 UTC corresponding to 11:50 a.m. local time.

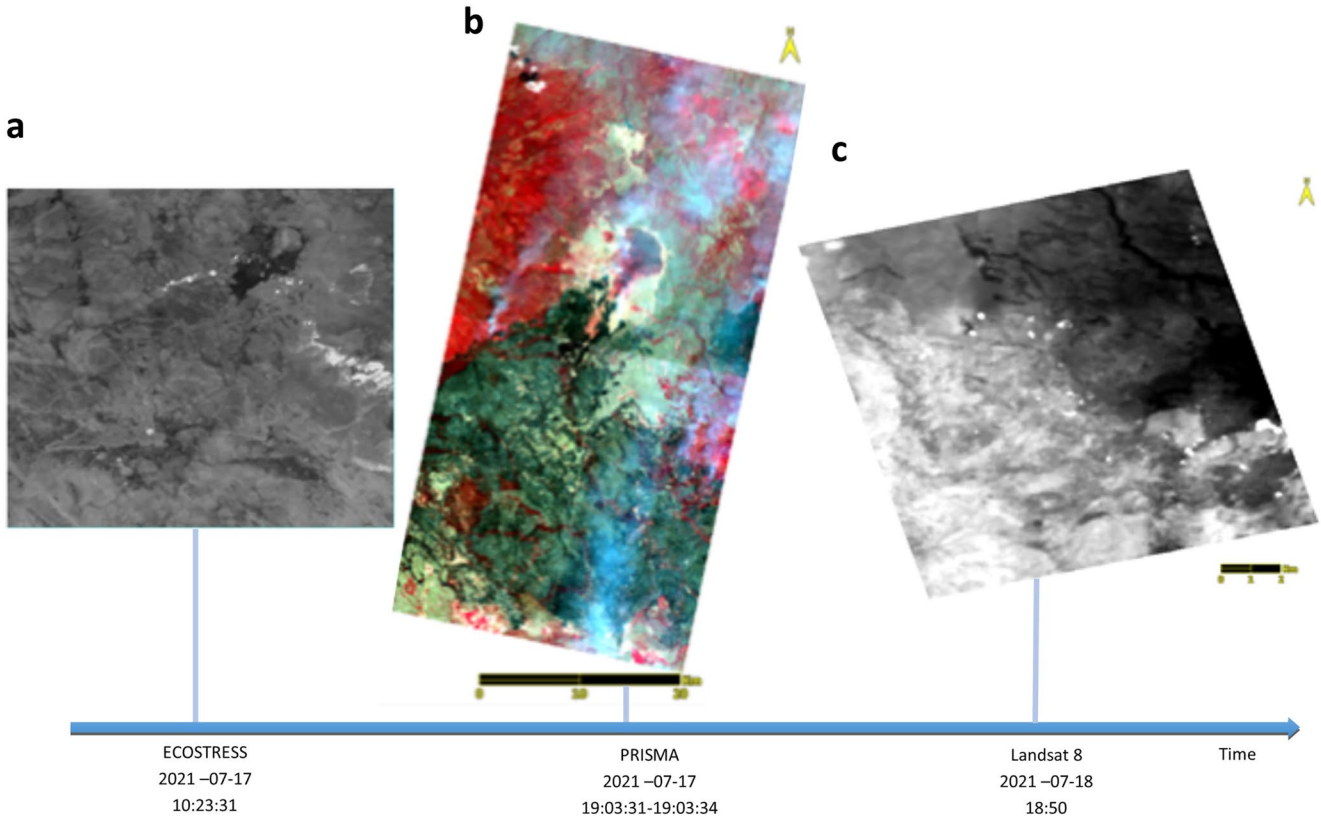

Figure 2. (a) ECOSTRESS temperature map acquired 9 hr before the PRISMA acquisition (b) PRISMA false colors two images North and South composition which includes both visible and infrared light captured a large portion of burn scar and active areas. The vegetation appears in shades of red and bare ground in shades of tan. The burned areas appear dark black and the smoke from the active fire front in blueish. (c) Landsat 8 daytime temperature map acquired 24 hr after the PRISMA acquisition.

3. Methods

3.1. HFDI

HFDI (Dennison & Roberts, 2009) allows the identification of active fire locations using specific bands in the SWIR hyperspectral range. The algorithm was developed by Dennison using airborne AVIRIS hyperspectral data (Dennison & Roberts, 2009) to produce accurate results in detecting pixels with fire. The HFDI is defined as:

$$\mathrm{HFDI} = \frac{L_{2430} - L_{2060}}{L_{2430} + L_{2060}} \tag{2}$$

where L_{2430} and L_{2060} are the spectral radiances at two specific SWIR bands around 2,430 and 2,060 nm expressed in $\mathrm{Wm^{-2}\ sr^{-1}\ \mu m^{-1}}$. These two bands were found to provide the best performance using AVIRIS spectral data (Dennison & Roberts, 2009; Matheson & Dennison, 2012). The HFDI was shown to be valuable as a detection index from space as well (Amici & Piscini, 2021; Waigl et al., 2019). In this study the PRISMA wavelengths 2,061 and 2,428 nm were chosen as the closest to the Dennison's best choice. In order to identify the active fire front, a thresholding approach is applied. The selection of the threshold required assumptions to be made and are discussed in the following session.

3.1.1. Threshold Selection

The HFDI index was initially derived by Dennison and Roberts (2009) who performed a comprehensive sensitivity analysis to identify the best bands combination and derive the threshold for separating burning from not burning pixels. They used airborne data from the AVIRIS sensor which covered a spectral range between 370 and 2,510 nm with 10 nm bandwidth (Green et al., 1998). They tested the HFDI sensitivity to elevation, atmospheric gases, atmospheric pathlength, solar zenith angle and water vapor. They tested the sensitivity of HFDI between

0 and 3 km (Dennison & Roberts, 2009) and the solar zenith angle between 0° and 75°. Because PRISMA's maximum angle is 20.7° (PRISMA User Manual - Issue 1.2, 2020), the dependency of HFDI from elevation may be assumed of second order. Because of HFDI utilizes bands which are subject to atmospheric contribution, this can influence the HFDI.

Diverse empirical approaches have been used in past studies to select the critical threshold to separate burning from not burning (Dennison & Roberts, 2009). In this study, the separation of burning and not burning is useful for the selection of the buffer zone for the temperature retrieval.

The first approach consistent with the literature considers the whole values in the image and through visual selection by sliding to adjust the value of the threshold upward until no pixels outside the apparent fire area are detected as burning. The second approach analyses the PRISMA HFDI values in correspondence with unburned, burned and mixed. The background study was conducted in the following way: eleven rectangular Region Of Interest (ROI) were selected in each of the two HFDI images within different categories such as vegetation, burned, bare soil, urban, cloud/smoke and water. For each ROI, the number of pixels (counts), minimum and maximum values, and the ROI's mean value and the standard deviation were retrieved.

3.2. Temperature Estimation

3.2.1. Description of the Methodology

Hyperspectral images can be used to estimate high temperatures of emitting sources. As reported in Dennison and Roberts (2009), at temperatures above 500 K, there is measurable emitted radiance in the shortwave infrared, that is, the spectral region from 1,400 to 2,500 nm which is detected by PRISMA. In this work, we employ an approach based on the technique presented by Dennison in Veraverbeke et al. (2018), even though some implementation differences have been introduced and they which will be explained later.

Temperature estimation can be attained by using the PRISMA level 2B images, that is, the bottom of atmosphere (BOA) radiance requested on the online portal and directly processed by ASI, and a linear mixture model. The pixel signal is expressed as a function of the wavelength λ and can be approximated by the linear mixture (LM) signal L_{LM}. This approximation is a weighted combination of m background signals $L_{j,\mathrm{bkg}}$ and n sources $L_{\mathrm{fire}}(T_i)$, $i = 1, 2, \ldots, n$, modeled as Planck gray body at temperature T_i,

$$L_{\mathrm{fire}}(T_i) = \frac{2\varepsilon hc^2}{\lambda^5(e^{(hc/k\lambda T_i)} - 1)} \tag{3}$$

where $\varepsilon \in (0, 1)$ is the emissivity, $c = 2.99792458 \cdot 10^8$ m/s is the speed of light, $h = 6.62607015 \cdot 10^{-34}$ Js is Planck's constant, and $k = 1.380649 \cdot 10^{-23}$ J·K^{-1} is Boltzmann's constant. The linear mixture signal L_{LM} is thus given as

$$L_{\mathrm{LM}} = \sum_{i=1}^{n} p_{i,\mathrm{fire}} L_{\mathrm{fire}}(T_i) + \sum_{j=1}^{m} p_{j,\mathrm{bkg}} L_{j,\mathrm{bkg}}, \tag{4}$$

where the weight parameters $p_{i,\mathrm{fire}}$ and $p_{j,\mathrm{bkg}}$ are defined such that $\sum_{i=1}^{n} p_{i,\mathrm{fire}} + \sum_{j=1}^{m} p_{j,\mathrm{bkg}} = 1$. A least square method is used to estimate the parameters $p_{i,\mathrm{fire}}$, $p_{j,\mathrm{bkg}}$ and the temperatures T_i.

3.2.2. Introduced Novelties

The differences with respect to the original method proposed in Waigl et al. (2019) are:

1. The background signals $L_{j,\mathrm{bkg}}$ are selected directly from the image, not from an external spectral library
2. The BOA radiance is used instead of the top of atmosphere (TOA) radiance.

The selection of the $L_{j,\mathrm{bkg}}$ signals should be done carefully, as they must not contain "hot pixels," that is, signals associated to hot temperatures. Indeed, in this case the background signal would absorb the contribution of the emitting source $L_{\lambda}(T_i)$, thus leading to an invalid and wrong estimation. Our selection is based on the preliminary analysis based on the HFDI, as discussed in Section 3.1. Accordingly, the background signals are chosen within the pixels having HFDI less than a user-defined threshold, with those choices discussed in Sections 4.1 and 4.2.

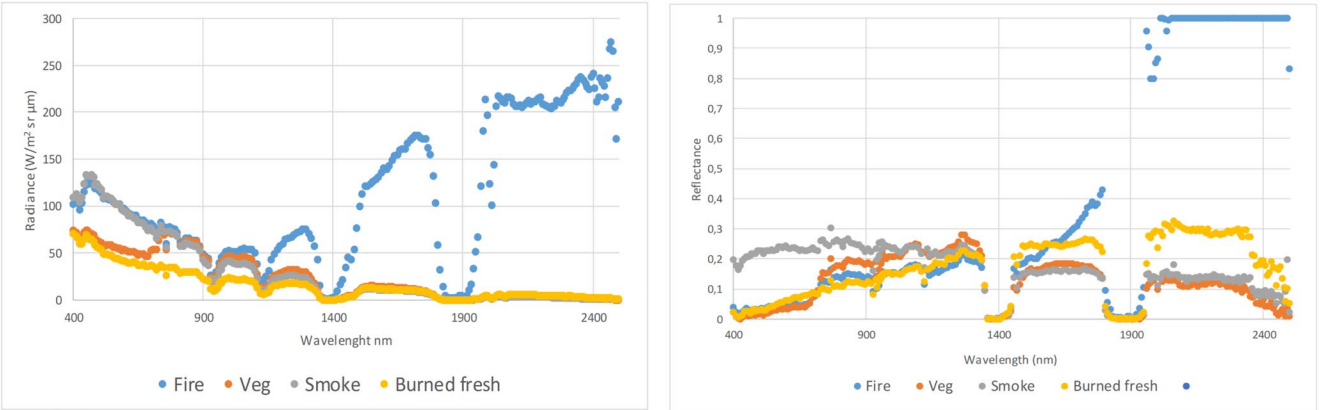

Figure 3. PRISMA Level 1 Spectral radiance of Fire, Vegetation (Veg), Smoke and freshly burned (Burned fresh) (a), and corresponding reflectance spectra (b).

To perform a temperature estimation, we solve Equation 4 N times, selecting each time m random background points within those having the proper HFDI. This approach is robust against the uncertainty in the knowledge of the true signal mixture as the temperature value is provided by averaging the N estimations. Moreover, it allows us to provide an *a-posteriori* confidence interval of the result. It is also noteworthy that choosing the background signal directly from the image maximizes the correlation between the analyzed spectrum with the ones used as background. Indeed, according to the first law of geography, stated by Waldo Tobler as "everything is related to everything else, but near things are more related than distant things" (Tobler, 1970), we expect to properly estimate the background signal of the pixel of interest by looking at nearby pixels.

Regarding the differences between using TOA or BOA signal, PRISMA allows the users to download both TOA and BOA radiance products (see Section 2.2.1 for further details). Since the BOA radiance is already processed by ASI using MODTRAN (PRISMA Documentation Area, 2020), this choice simplifies the overall approach as the Planck curve does not need to be processed to take care of the atmosphere, as was done in Waigl et al. (2019). The only processing required for the Planck curve is to set to zero the signal in correspondence of the SWIR atmospheric water absorption bands.

Finally, it is worth mentioning that in all the previous studies concerning temperature estimation from hyperspectral data, the reference emission model was the Planck black body was $\varepsilon = 1$. Consistent with the literature, and given that it is not easy to provide a proper emissivity to each pixel of the PRISMA image, in this work we will use $\varepsilon = 1$, and possible investigations for the case of the gray body hypothesis will be addressed in future works.

3.2.3. Practical Implementation and Limitation

Even though PRISMA has been demonstrated to provide users with a quality image which is not comparable with previous similar mission EO1.Hyperion (e.g., PRISMA signal-to-noise ratio reaches 200:1 in the VNIR channels and 100:1 in the SWIR channels, see PRISMA Documentation Area, (2020) for further information), PRISMA was not specifically designed to detect hot events. As a consequence, when detecting a signal from a wildfire, what happens most of the time is that the signal saturates after about 1,900 nm. To show this issue, the PRISMA radiance and reflectance spectral behavior are reported in Figure 3 in correspondence of four pixel categories: fire, vegetation, smoke, and freshly burned. The spectral signatures of vegetation, smoke, and freshly burned classes behave in an expected way, whereas a typical saturation problem can be appreciated from the radiance of the fire pixel (blue dots). Indeed, the fire signal behaves in an unexpected way as it goes almost flat, instead of increasing, after the atmospheric absorption interval around 1,900 nm. In a similar fashion, the reflectance saturates at its maximum value, which is 1, indicating that overall sensed signal is higher that the nominal one received by the Earth from the Sun. As a consequence, the proposed algorithm cannot use all bands in the SWIR wavelengths, and the interval 1,400–1,800 nm has been recognized as the most promising one by analyzing several spectra of active fire pixels. It is noteworthy that this is only a limitation of the current technology implemented on PRISMA and other future sensors could increase the saturation range of applicable wavelengths.

Regarding the overall computational effort, even though the single estimation is not time consuming (see results in Section 4.2) the averaging procedure increases the computational effort (even though a CPU parallelization has

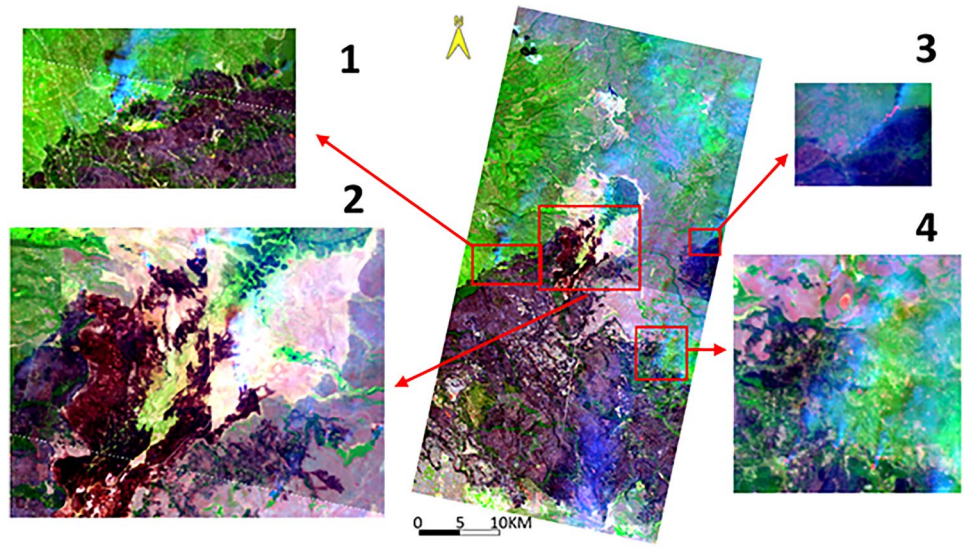

Figure 4. Four areas of interest for running the temperature estimation algorithm. The image is displayed in false colors, where Red is 1646.97 nm, Green is 855.18 nm and Blue is 579.35 nm.

been used to optimize the entire process). As a consequence, to reduce the time to get the temperature maps, we turned our attention into four sub-regions of interest, which are shown in Figure 4.

3.3. Verification Analysis

Although the hyperspectral PRISMA data provide valuable information due to characteristics of its spectra, the 30 m horizontal resolution unavoidably includes mixes in land cover (i.e., fire over a fraction of the pixel) Enhancing the spatial resolution would help to support data interpretation and provide an indirect validation. For example, super-hot pixels associated with active wildfire covering most of the pixel would potentially glow and be seen in the VNIR at much higher spatial resolution. Because of a panchromatic image is acquired at 5 m spatial resolution, the application of a pansharpening algorithm has been utilized. Among the different algorithms available, the Gram Schimth has been selected as the one which perform better (Ghosh et al., 2014; Sabat-Tomala et al., 2020; Xiang et al., 2020) in terms of spectral characteristics preservation when operating at the (almost same) spectral range. The pansharpened image will be used against temperature map to verify hot spots at flaming temperature.

4. Results

4.1. Fire Detection Based on HFDI

The HFDI map was derived for the two PRISMA images (North and South) acquired over the Bootleg Fire.

Figure 5 shows the HFDI map and the 11 Region Of Interest (ROI) representative of different categories. Due to the characteristics of the mapped scene some of them have been chosen to be relatively homogeneous (i.e., Burned 1, Burned 2, Water) and some mixed comprising diverse categories. A polyline rather than a square was used to select the water category because of its angular shape.

Table 3 summarizes the counts and the HFDI values resulting from basic statistics (minimum, maximum mean and standard deviation) applied to the eleven ROI associated to different categories.

In the North image the mean values of HFDI background spans between −0.4700 (water) and −0.250-(mixed area type Burned Smoke Vegetation). We noticed that the values are consistent with values found in the literature for AVIRIS (Dennison & Roberts, 2009).

Dennison and Roberts (2009) found −0.179 as the ash-background threshold (for AVIRIS 4–16 m resolution) which appears similar to the values found in maximum values for Burnd 1 and Burned 2 in Table 3 (North image).

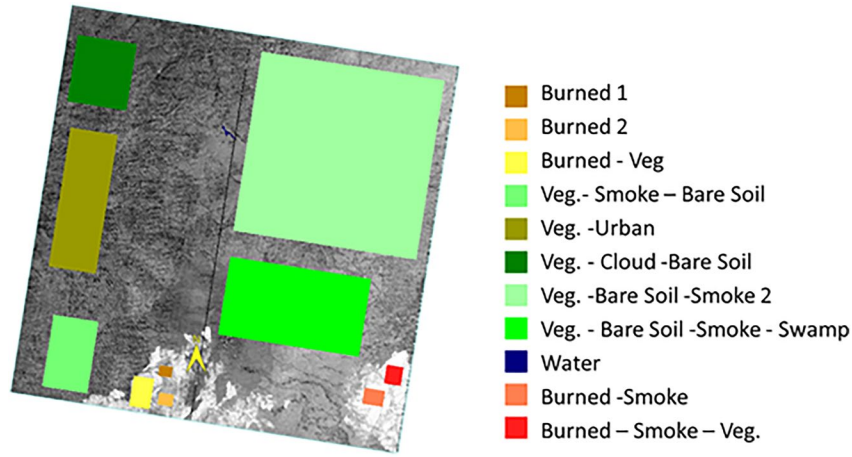

Figure 5. North HFDI image: region of interest (ROIs) selected for 11 different categories.

In addition, Dennison and Roberts (2009) suggested −0.1 as threshold for likely active fire pixels. However in this image the values of HFDI for the water body in the image span between min −1.00 and max −0.1 suggesting a commission error would be introduced if the Dennison threshold would be applied to discriminate burning from not burning pixels.

Figure 6 shows the HFDI map and the 11 Region Of Interest (ROI) representative of different categories for the South Image.

Table 4 are the summarized counts and HFDI values resulting by applying the same statistic used previously but to a different area (South Image).

Following the comparative analysis of the background values of the two images (North and South) the −0.2 value for the HFDI threshold has been selected as up limit for no fire within the image.

However, this value is not to be considered the critical threshold to be used to separate not burning pixels from pixels likely to contain active fire (Dennison & Roberts, 2009) which is evaluated empirically and can likely be around the −0.1 value indicated by Dennison and Roberts (2009) using different parameters, sensors characteristics (i.e., spatial and spectral resolution), and atmospheric conditions.

Table 3
PRISMA North Image

Area type	Count	Min	Max	Mean	Stdev
Burned 1	918	−0.457	−0.169	−0.327	0.034
Burned 2	1178	−0.439	−0.212	−0.335	0.031
Burned–Veg	4,134	−0.676	0.263	−0.309	0.051
Veg–Smoke–Soil	21,460	−0.742	−0.236	−0.428	0.044
Veg–Urban	43,798	−0.953	−0.175	−0.440	0.005
Veg Cloud Bare Soil	26,316	−1.00	0.360	−0.454	0.057
Veg Bare soil Smoke 2	218,999	−0.703	−0.222	−0.392	0.038
Veg Bare Soil Smoke–Swamp	73,164	−1.000	−0.042	−0.392	0.047
Water	161	−1.00	−0.109	−0.4700	0.185
Burned smoke	2173	−0.476	−0.033	−0.269	0.029
Burned Smoke Veg	2064	−0.444	−0.122	−0.250	0.004

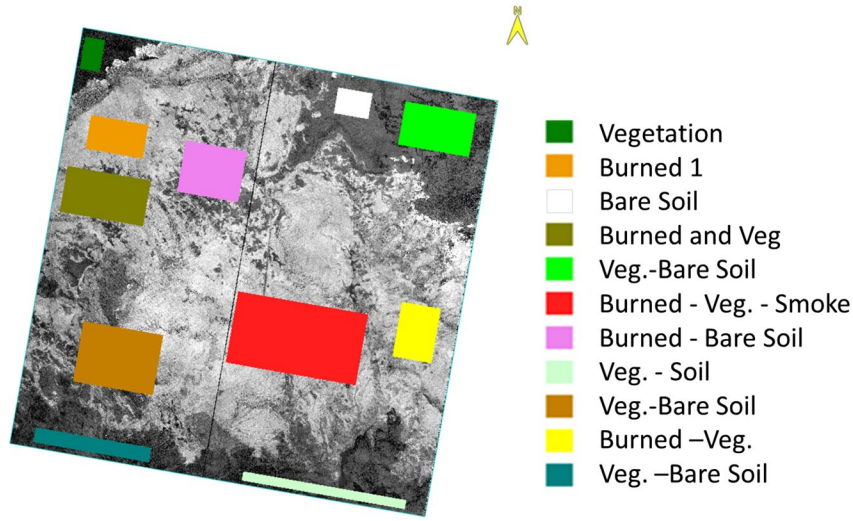

Figure 6. South HFDI image: region of interest (ROIs) selected for 11 different categories.

4.2. Temperature Retrieval

The experimental results of the procedure described in Section 3.2 are reported here. For the practical implementation of the algorithm, the user-defined parameters have been set as $n = 1$, $m = 20$, with a number of estimations $N = 15$ for each pixel. The HFDI threshold to choose for the background pixels has been set equal to -0.2. This value comes from the previous analysis and considers an additional margin to make the analysis more conservative and consistent.

First, the temperature estimations for the four areas identified in Figure 4 are reported in Figure 7. Here, one can appreciate how the peak temperature values are consistent with the expected results. All temperatures below about 600 K don't have any physical meaning, and are simply mathematical results from the optimization procedure obtained when the fire signal is too low compared to other signal sources. Most of the active fire pixels are detected in the region 4, where many locations above 1000 K are identified. For this Region 4, we also show more detailed results in Figures 8a and 8b. Here, one can appreciate the quantity and distribution of the most reliable estimations, that is, those pixels having a temperature estimate greater than 600 K. As can be seen, only a few pixels are above this threshold, and this result is consistent with the fact that PRISMA only measures infrared signal up to 2,400 nm, thus being limited to measuring only very hot sources (where the saturation also reduces the useful signal up to about 1,800 nm). Another interesting result is represented by the values of the p_{fire} coefficients (Figure 8c), where one can see that the mixture coefficients of the active fire pixels are quite high and close to one. Finally, in Figure 8d we report the ratio of temperature standard deviation over mean value (these values are retrieved from the 15 temperature evaluations performed for each pixel) which is an indicator of the precision of the generic estimation. In this case, values are generally low the temperature is very high.

The average computational time for the temperature estimation algorithm is 1.57×10^{-2} seconds on a Windows 11 PC x64, Intel(R) Core (TM) i7-9750H CPU @ 2.60 GHz, 2592 Mhz, 6 core, 12 processori logici, 16 GB RAM.

Table 4
PRISMA South Image

Area type	Count	Min	Max	Mean	Stdev
Vegetation	3,696	−0.662	−0.315	−0.425	0.037
Burned 1	11,178	−0.419	−0.206	−0.296	0.002
Bare soil	5,146	−0.429	−0.285	−0.361	0.016
Burned and Veg–	22,110	−0.561	−0.173	−0.313	0.036
Veg.–Bare soil–Smoke	17,784	−0.578	−0.278	0.0379	0.032
Burned–Veg.–Smoke	53,523	−0.599	−0.129	−0.297	0.031
Burned–Bare soil	18,081	−0.580	−0.169	−0.333	0.047
Veg–Soil	8,646	−0.722	−0.267	−0.413	0.043
Burned Veg;–Bare Soil	27,840	−0.540	−0.113	−0.331	0.0517
Burned–Veg	12,314	−0.448	−0.197	−0.298	0.028
Veg–Bare Soil	9,765	−0.908	−0.165	−0.412	0.049

Note. The average of maximum values in the South image is −0.21.

4.3. Comparative Analysis

A qualitative comparative analysis of the thermal maps produced by PRISMA, ECOSTRESS and Landsat 8 shows the fire's change through time. Figure 9 shows the thermal behavior of the fire front in ROI number 4.

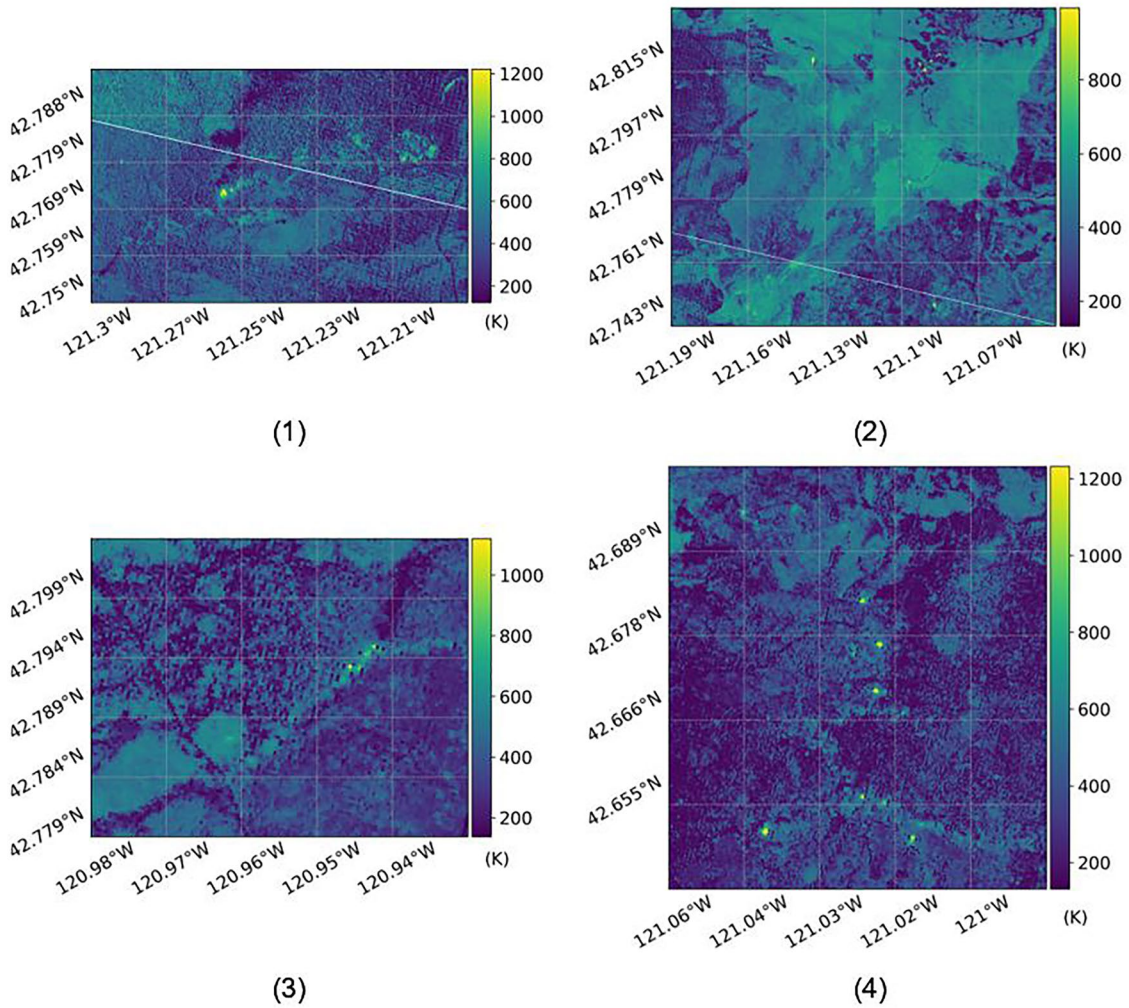

Figure 7. Temperature maps for the 4 region of interest (ROIs).

The ECOSTRESS hot spots (Figure 9a) corresponding to active likely flaming pixels (blue color) are located in the north part of the image while 9 hr later the hot spots detected by PRISMA (blue color) appear to be located in the center part of ROI number 4 suggesting that the burning areas previously mapped by ECOSTRESS have are now smaller.

The PRISMA high-resolution pansharpened image (Figure 9c) is shown as a false color composite NIR-SWIR (972, 876, 770 nm). It has been used to locate areas where the predominant fire component in some pixels reach temperatures greater than 1000 K. The black arrows in Figure 9c point to 4 glowing pixels corresponding to biomass flaming and consisted with the high temperatures in Figure 9b. This comparison, allows us to provide an indirect qualitative validation of the temperature retrieval model we have used. Finally the Landsat 8 temperature map (Figure 9d) shows how the fire front has continued to change, showing a fragmented fire front with hot spots in different areas of the image.

5. Discussion

This work demonstrates the usefulness of using hyperspectral images, specifically PRISMA data, to provide detailed analysis of wildfire scenarios.

The Hyperspectral Fire Index was derived by using comparative PRISMA wavelengths to those in Dennison and Roberts (2009). Although, the discussion of performance of HFDI is beyond the purpose of this paper, the results

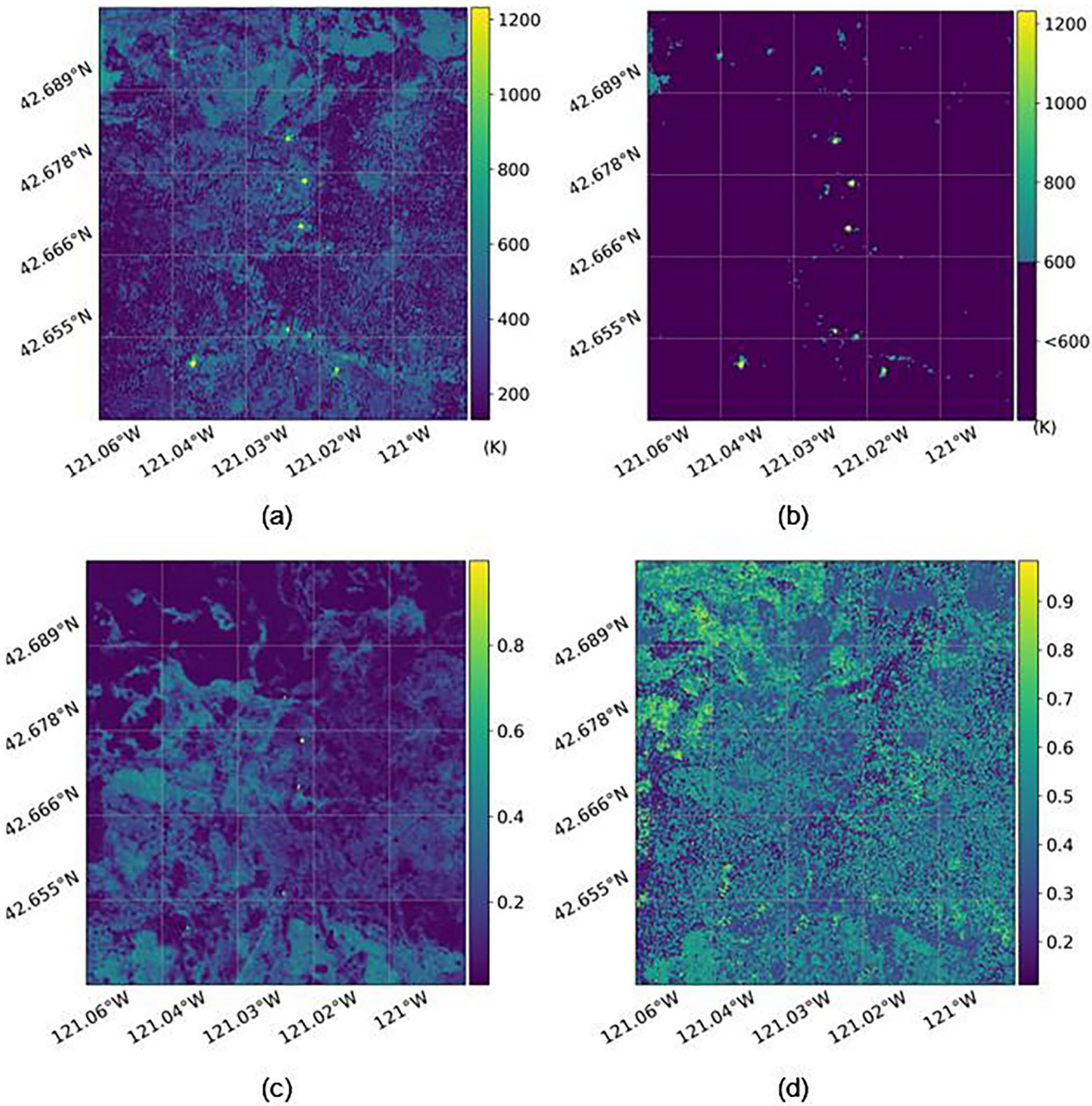

Figure 8. Considering the region of interest (ROI) number 4 from Figure 7, (a) temperature map, (b) temperature map with 600 K mask, (c) *p* coefficients, and (d) ratio between standard deviation and mean temperature.

demonstrated that the HFDI map allows the location of the active fire front (soft classification). The range variation of the HFDI values was found in agreement with the values obtained by Dennison and Roberts (2009) using AVIRIS (resolution spanning between 5 and 20 m depending on flight altitude). This can potentially be related to different reasons including (but not limited to) the good PRISMA performance in terms of radiance signal to noise, the PRISMA bands for the HFDI are almost identical to the AVIRIS ones, and the 30 m spatial resolution of PRISMA is relatively close to the 20 m coarser resolution of AVIRIS.

The comparison with the thermal maps acquired temporally close to the PRISMA acquisition (ECOSTRESS and Landsat 8) show the potential for virtual constellations to characterize the wildfire thermal behavior. For example,

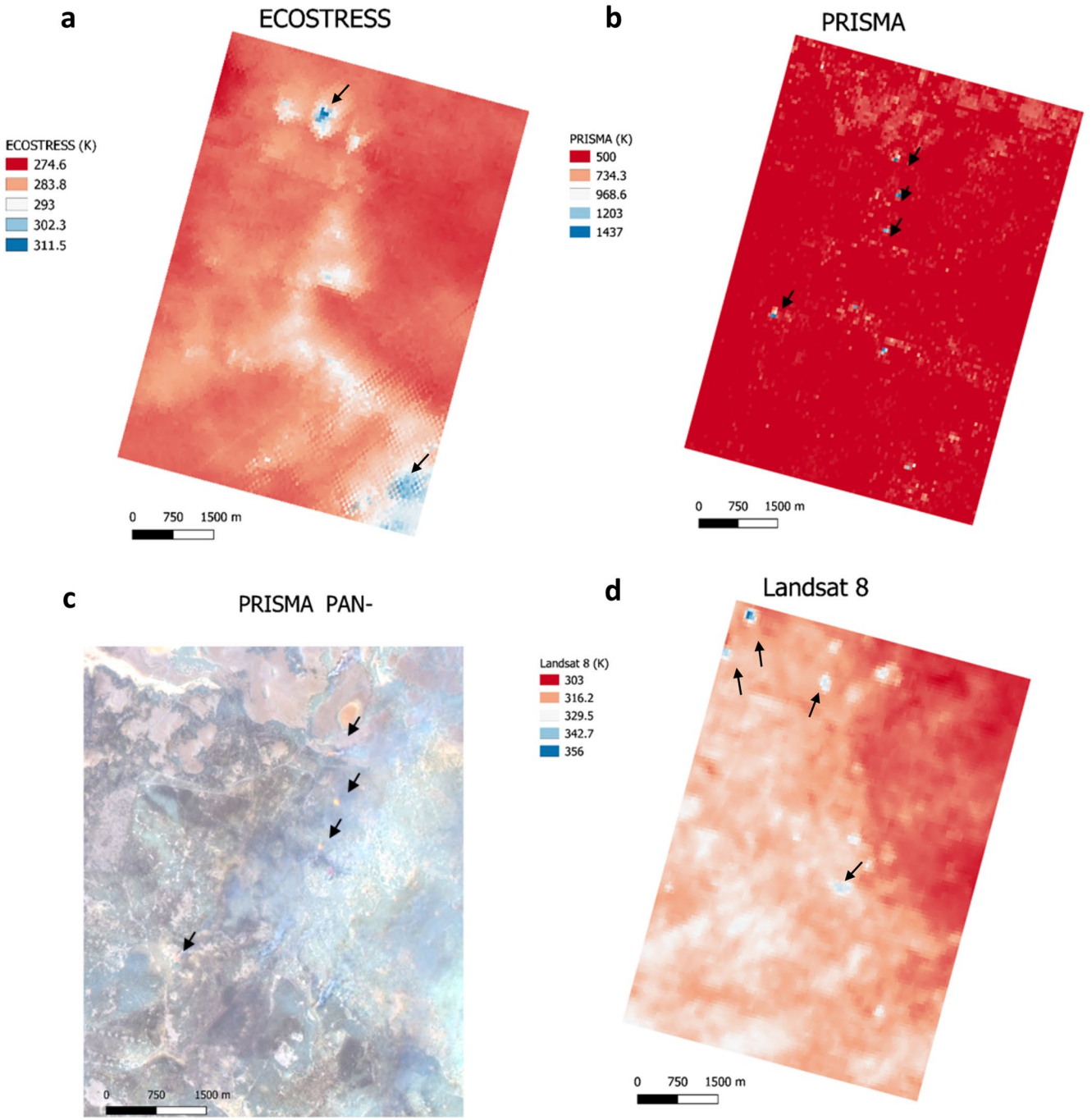

Figure 9. (a) ECOSTRESS LST temperature map in Kelvin, with high temperature hot spots (light blue, black arrows) located in the North and South/East part of the scene; (b) PRISMA temperature map for locations >500 K. Black arrows point at the pixels with temperature greater than 1000 K; (c) RGB false color composite in NIR-SWIR bands respectively at: 972, 876, 770 nm of pansharpened PRISMA imagery at 5 m resolution; the black arrows point at the same pixels highlighted in (b) and appear glowing as characterized by flaming fires; (d) Landsat 8 thermal map shows the wildfire front highly fragmented with hot spots (light blue color, clack arrow) sparsed the image.

the PRISMA and ECOSTRESS images showed clear movement of the fire front, highlighted by change in the hot spots. The Landsat 8 image taken 1 day later shows continued temporal evolution of the fire front as well as new hot spots and areas burned. While during the Bootleg Fire ECOSTRESS data proved to be useful for operational decision-making and incorporated in the New Wildfire Response Tool delivered by NASA (ECOSTRESS Data Incorporated Into New Wildfire Response Tool NASA, n.d.), we suggest that the synergetic use of ECOSTRESS,

PRISMA, LANDSAT and other hyperspectral sensors (i.e., EnMAP) has the potential for enhancing the available information for operational activities in terms of identifying hot flaming and smouldering areas for the response team deployment, airborne and ground fire suppression strategies, and evaluating the fire damage to infrastructure, buildings and ecosystems.

The results reported in this work are particularly relevant if we think to the limitations of the input data. Indeed, even though PRISMA is a very innovative and unique sensor, the hyperspectral instrument was not designed for temperature estimation. As a consequence, the infrared wavelengths in the SWIR channels are limited to about 2,400 nm, which is not enough to estimate room temperature or low temperatures in general.

On the other hand, the saturation effect could be hopefully minimized in next generations of hyperspectral sensors which could have an increased dynamic range by using for example, a tunable integration time. Nonetheless, this work demonstrates that temperature estimation of extreme hot events as wildfires is a feasible application, with reliable results and little computational effort. Hence, there is a possibility to provide a spatially bounded, high-spatial and spectral resolution information about high temperature wildfire events which is complementary to worldwide-coverage of low/medium resolutions temperature maps offered by other thermal instruments.

An ideal validation would involve coincident in situ and/or airborne-satellite collections with a PRISMA acquisition. However, this kind of experiments still remains rare due to numerous challenges linked to their realization (Wooster et al., 2021). In our case, because of a lack of independent thermal data contemporaneous to PRISMA, a consistent qualitative validation of the temperature estimation results has been presented. Results of the qualitative analysis are in line with the ECOSTRESS and Landsat products. The high-resolution image analysis of the PRISMA pan-sharpened scene proves that the sharpened high temperature pixels remain identifiable. The temperature estimations are also in line with expectations, and illustrate the ability to discriminate active fires from the background signal. As such, the technique proposed in this paper can be used as a complementary tool along with other established methodologies. To note that the use of virtual constellation of different satellites (which would include new hyperspectral missions such as the recently launched EnMap) likely enables approaches to increase both the spatial and temporal resolution of detection and temperature products.

6. Conclusion

This paper analyzed wildfire scenarios as captured from the hyperspectral camera on board the PRISMA mission. This work investigated the application of the Hyperspectral Fire Index to the PRISMA data, and the evaluation of the active fire temperature by using a linear mixture analysis. In both cases, we demonstrated that Hyperspectral Fire Index derived for the Bootleg Fire in Oregon (USA) provides results consistent with historical AVIRIS results in the literature (Dennison & Matheson, 2011; Dennison & Roberts, 2009), and allow the mapping of the active fire areas. Both near to zero and positive values of HFDI (>-0.1) corresponds to pixels likely to contain active fire (Dennison & Roberts, 2009) and high temperature values corresponding to flaming active (>1000 K) have been identified. Pansharpening was also used for verification of very-hot pixels. Qualitative comparison of PRISMA temperature versus ECOSTRESS and Landsat 8 acquired near to PRISMA acquisition showed the potential offered by utilizing multiple satellites over the same area. Specifically, they describe the fire behavior by improved the temporal revisit time with a potential positive impact in term of wildfire monitoring as well as monitoring critical infrastructure or sensitive environments.

Data Availability Statement

The PRISMA data used for this study cannot be distributed according to the Italian Space Agency policy. However, readers interested in reproducing the results can download the images on their own by registering at the ASI-PRISMA portal https://prisma.asi.it.

- The python software used in this work as well as the results of the temperature analysis of the study produced with both python and ENVI© are available at Zenodo DOI: https//doi.org/10.5281/zenodo.7273879
- The data set related to the ENVI© processing can be found under Zenodo DOI: https//doi.org/10.5281/zenodo.7271523
- The ECOSTRESS data can be accessed at https://ecostress.jpl.nasa.gov/data.
- The Landsat 8 data can be accessed at https://earthexplorer.usgs.gov/.

Acknowledgments
Italian Space Agency (ASI) NASA and USGS are thanked for providing free data access. Part of this study has been conducted within the Project "Sviluppo di prodotti iperspettrali prototipali evoluti" funded by ASI.

References

Abatzoglou, J. T., & Williams, A. P. (2016). Impact of anthropogenic climate change on wildfire across Western US forests. *Proceedings of the National Academy of Sciences of the United States of America*, *113*(42), 11770–11775. https://doi.org/10.1073/PNAS.1607171113/SUPPL_FILE/PNAS.1607171113.SD03.CSV

Amici, S., & Piscini, A. (2021). Exploring prisma scene for fire detection: Case study of 2019 bushfires in ben Halls Gap National Park, NSW, Australia. *Remote Sensing*, *13*(8), 1410. https://doi.org/10.3390/rs13081410

Amici, S., Wooster, M. J., & Piscini, A. (2011). Multi-resolution spectral analysis of wildfire potassium emission signatures using laboratory, airborne and spaceborne remote sensing. *Remote Sensing of Environment*, *115*(8), 1811–1823. https://doi.org/10.1016/j.rse.2011.02.022

Ananasso, C., Bianco, G., Candela, L., Dini, L., Garramone, L., Loizzo, R., et al. (2009). Italian Space Agency pilot projects to support disaster management and environmental monitoring. In *Proceedings, 33rd international symposium on remote sensing of environment*. ISRSE.

Andreae, M. O. (2019). Emission of trace gases and aerosols from biomass burning - An updated assessment. *Atmospheric Chemistry and Physics*, *19*(13), 8523–8546. https://doi.org/10.5194/ACP-19-8523-2019

Andreae, M. O., & Merlet, P. (2001). Emission of trace gases and aerosols from biomass burning. *Global Biogeochemical Cycles*, *15*(4), 955–966. https://doi.org/10.1029/2000GB001382

Archibald, S., Lehmann, C. E. R., Belcher, C. M., Bond, W. J., Bradstock, R. A., Daniau, A. L., et al. (2018). Biological and geophysical feedbacks with fire in the Earth system. *Environmental Research Letters*, *13*(3), 033003. https://doi.org/10.1088/1748-9326/AA9EAD

Auld, T. D., & O'Connell, M. A. (1991). Predicting patterns of post-fire germination in 35 eastern Australian Fabaceae. *Australian Journal of Ecology*, *16*(1), 53–70. https://doi.org/10.1111/j.1442-9993.1991.tb01481.x

Barducci, A., Guzzi, D., Marcoionni, P., & Pippi, I. (2004). Comparison of fire temperature retrieved from SWIR and TIR hyperspectral data. *Infrared Physics & Technology*, *46*(1–2), 1–9. https://doi.org/10.1016/j.infrared.2004.03.001

Barmpoutis, P., Papaioannou, P., Dimitropoulos, K., & Grammalidis, N. (2020). A review on early forest fire detection systems using optical remote sensing. *Sensors*, *20*(22), 6442. https://doi.org/10.3390/s20226442

Boardman, J. W., & Green, R. O. (2000). Exploring the spectral variability of the Earth as measured by AVIRIS in 1999 - NASA Technical Reports Server (NTRS). Retrieved from https://ntrs.nasa.gov/citations/20060033835

Boulet, P., Parent, G., Acem, Z., Collin, A., & Séro-Guillaume, O. (2011). On the emission of radiation by flames and corresponding absorption by vegetation in forest fires. *Fire Safety Journal*, *46*(1–2), 21–26. https://doi.org/10.1016/J.FIRESAF.2010.03.006

Bright, B. C., Hudak, A. T., Kennedy, R. E., Braaten, J. D., & Henareh Khalyani, A. (2019). Examining post-fire vegetation recovery with Landsat time series analysis in three Western North American forest types. *Fire Ecology*, *15*(1), 1–14. https://doi.org/10.1186/S42408-018-0021-9/TABLES/7

Candela, L., Formaro, R., Guarini, R., Loizzo, R., Longo, F., & Varacalli, G. (2016). The PRISMA mission. *International Geoscience and Remote Sensing Symposium (IGARSS)*. https://doi.org/10.1109/IGARSS.2016.7729057

Carmona, E., Avbelj, J., Alonso, K., Bachmann, M., Cerra, D., Eckardt, A., et al. (2017). Data processing for the space-based desis hyperspectral sensor. *International Archives of the Photogrammetry, Remote Sensing and Spatial Information Sciences - ISPRS Archives*, 271–277. https://doi.org/10.5194/isprs-archives-XLII-1-W1-271-2017

Cawse-Nicholson, K., Townsend, P. A., Schimel, D., Assiri, A. M., Blake, P. L., Buongiorno, M. F., et al. (2021). NASA's surface biology and geology designated observable: A perspective on surface imaging algorithms. *Remote Sensing of Environment*, *257*, 112349. https://doi.org/10.1016/j.rse.2021.112349

Chuvieco, E., Mouillot, F., van der Werf, G. R., San Miguel, J., Tanasse, M., Koutsias, N., et al. (2019). Historical background and current developments for mapping burned area from satellite Earth observation. *Remote Sensing of Environment*, *225*, 45–64. https://doi.org/10.1016/J.RSE.2019.02.013

Coppo, P., Brandani, F., Faraci, M., Dami, M., Chiarantani, L., Ponticelli, B., et al. (2020). Leonardo spaceborne infrared payloads for Earth observation: SLSTRs for copernicus sentinel 3 and PRISMA hyperspectral camera for PRISMA satellite. *Applied Optics*, *59*(23), 6888. https://doi.org/10.1364/ao.389485

Csiszar, I. A., Morisette, J. T., & Giglio, L. (2006). Validation of active fire detection from moderate-resolution satellite sensors: The MODIS example in Northern Eurasia. *IEEE Transactions on Geoscience and Remote Sensing*, *44*(7), 1757–1764. https://doi.org/10.1109/TGRS.2006.875941

Davies, D., Ederer, G., Olsina, O., Wong, M., Cechini, M., & Boller, R. (2020). NASA's fire information for resource management system (FIRMS): Near real-time global fire monitoring using data from MODIS and VIIRS. NASA Technical Reports GSFC-E-DAA-TN73770.

Dennison, P. E. (2006). Fire detection in imaging spectrometer data using atmospheric carbon dioxide absorption. *International Journal of Remote Sensing*, *27*(14), 3049–3055. https://doi.org/10.1080/01431160600660871

Dennison, P. E., & Matheson, D. S. (2011). Comparison of fire temperature and fractional area modeled from SWIR, MIR, and TIR multispectral and SWIR hyperspectral airborne data. *Remote Sensing of Environment*, *115*(3), 876–886. https://doi.org/10.1016/j.rse.2010.11.015

Dennison, P. E., & Roberts, D. A. (2009). Daytime fire detection using airborne hyperspectral data. *Remote Sensing of Environment*, *113*(8), 1646–1657. https://doi.org/10.1016/J.RSE.2009.03.010

Dickinson, M. B., & Johnson, E. A. (2001). Chapter 14 - fire effects on trees, forest fire behavior and ecological effects (pp. 477–525).

Domenikiotis, C., Dalezios, N. R., Loukas, A., & Karteris, M. (2002). Agreement assessment of NOAA/AVHRR NDVI with Landsat TM NDVI for mapping burned forested areas. *International Journal of Remote Sensing*, *23*(20), 4235–4246. https://doi.org/10.1080/01431160110107707

Domenikiotis, C., Loukas, A., & Dalezios, N. R. (2003). The use of NOAA/AVHRR satellite data for monitoring and assessment of forest fires and floods. *Natural Hazards and Earth System Science*, *3*(1/2), 115–128. https://doi.org/10.5194/nhess-3-115-2003

EarthExplorer. (n.d.). United States Geological Survey (USGS) Website data portal. Retrieved from https://earthexplorer.usgs.gov/

ECOSTRESS Data Incorporated Into New Wildfire Response Tool NASA. (n.d.). Retrieved from https://www.nasa.gov/feature/jpl/ecostress-data-incorporated-into-new-wildfire-response-tool

Engebretson, C. (2022). Landsat collection 2 (C2) U.S. Analysis Ready Data (ARD) Data Format Control Book (DFCB). Retrieved from https://www.usgs.gov/media/files/landsat-collection-2-us-analysis-ready-data-dfcb

Freeborn, P. H., Wooster, M. J., Hao, W. M., Ryan, C. A., Nordgren, B. L., Baker, S. P., & Ichoku, C. (2008). Relationships between energy release, fuel mass loss, and trace gas and aerosol emissions during laboratory biomass fires. *Journal of Geophysical Research*, *113*(D1), 1301. https://doi.org/10.1029/2007JD008679

Galeazzi, C., Sacchetti, A., Cisbani, A., & Babini, G. (2008). The prisma program. *International Geoscience and Remote Sensing Symposium (IGARSS)*. https://doi.org/10.1109/IGARSS.2008.4779667

Ghosh, A., Fassnacht, F. E., Joshi, P. K., & Kochb, B. (2014). A framework for mapping tree species combining hyperspectral and LiDAR data: Role of selected classifiers and sensor across three spatial scales. *International Journal of Applied Earth Observation and Geoinformation*, *26*(1), 49–63. https://doi.org/10.1016/J.JAG.2013.05.017

Giglio, L., Csiszar, I., Restás, Á., Morisette, J. T., Schroeder, W., Morton, D., & Justice, C. O. (2008). Active fire detection and characterization with the advanced spaceborne thermal emission and reflection radiometer (ASTER). *Remote Sensing of Environment*, *112*(6), 3055–3063. https://doi.org/10.1016/J.RSE.2008.03.003

Green, R. O., Eastwood, M. L., Sarture, C. M., Chrien, T. G., Aronsson, M., Chippendale, B. J., et al. (1998). Imaging spectroscopy and the airborne visible/infrared imaging spectrometer (AVIRIS). *Remote Sensing of Environment*, *65*(3), 227–248. https://doi.org/10.1016/S0034-4257(98)00064-9

Grutzen, P. J., & Andreae, M. O. (1990). Biomass burning in the tropics: Impact on atmospheric chemistry and biogeochemical cycles. *Science*, *250*(4988), 1669–1678. https://doi.org/10.1126/SCIENCE.250.4988.1669

Guanter, L., Kaufmann, H., Segl, K., Foerster, S., Rogass, C., Chabrillat, S., et al. (2015). The EnMAP spaceborne imaging spectroscopy mission for Earth observation. *Remote Sensing*, *7*(7), 8830–8857. https://doi.org/10.3390/rs70708830

Guarini, R., Loizzo, R., Facchinetti, C., Longo, F., Ponticelli, B., Faraci, M., et al. (2018). PRISMA hyperspectral mission products. *International Geoscience and Remote Sensing Symposium (IGARSS)*. https://doi.org/10.1109/IGARSS.2018.8517785

Hook, S., & Hulley, G. (2019). ECOSTRESS land surface temperature and emissivity daily L2 global 70 m V001. https://doi.org/10.5067/ECOSTRESS/ECO2LSTE.001

Johnston, J. M., Wooster, M. J., Paugam, R., Wang, X., Lynham, T. J., & Johnston, L. M. (2017). Direct estimation of Byram's fire intensity from infrared remote sensing imagery. *International Journal of Wildland Fire*, *26*(8), 668–684. https://doi.org/10.1071/WF16178

Kaufman, Y. J., Hobbs, P. V., Kirchhoff, V. W. J. H., Artaxo, P., Remer, L. A., Holben, B. N., et al. (1998). Smoke, Clouds, and Radiation-Brazil (SCAR-B) experiment. *Journal of Geophysical Research*, *103*(D24), 31783–31808. https://doi.org/10.1029/98JD02281

Kaufman, Y. J., Justice, C., Flynn, L., Kendall, J., Prins, E., Ward, D. E., et al. (1998). Monitoring global fires from EOS-MODIS. *Journal of Geophysical Research*, *97*(D13), 14581. https://doi.org/10.1029/92jd00275

Kaufman, Y. J., Setzer, A., Justice, C., Tucker, C. J., Pereira, M. C., & Fung, I. (1990). Remote sensing of biomass burning in the tropics (pp. 371–399). https://doi.org/10.1007/978-3-642-75395-4_16

Kennard, D. K., Outcalt, K. W., Jones, D., & O'Brien, J. J. (2005). Comparing techniques for estimating flame temperature of prescribed fires. *Fire Ecology*, *1*(1), 75–84. https://doi.org/10.4996/FIREECOLOGY.0101075

Key, C. H., & Benson, N. C. (2006). LA-1 landscape assessment (LA) sampling and analysis methods - Lutes, Duncan C.; Keane, Robert E.; Caratti, John F.; Key, Carl H.; Benson, Nathan C.; Sutherland, Steve; Gangi, Larry J. 2006. FIREMON: Fire effects monitoring and inventory system. In *General Technical Reports RMRS-GTR-164-CD*.

Kohlenberg, A. J., Turetsky, M. R., Thompson, D. K., Branfireun, B. A., & Mitchell, C. P. J. (2018). Controls on boreal peat combustion and resulting emissions of carbon and mercury. *Environmental Research Letters*, *13*(3), 035005. https://doi.org/10.1088/1748-9326/AA9EA8

Loizzo, R., Ananasso, C., Guarini, R., Lopinto, E., Candela, L., & Pisani, A. R. (2016). *The prisma hyperspectral mission*. European Space Agency, (Special Publication) ESA SP.

Loizzo, R., Daraio, M., Guarini, R., Longo, F., Lorusso, R., Dini, L., & Lopinto, E. (2019). Prisma mission status and perspective. *International Geoscience and Remote Sensing Symposium (IGARSS)*. https://doi.org/10.1109/IGARSS.2019.8899272

Loizzo, R., Guarini, R., Longo, F., Scopa, T., Formaro, R., Facchinetti, C., & Varacalli, G. (2018). Prisma: The Italian hyperspectral mission. *International Geoscience and Remote Sensing Symposium (IGARSS)*. https://doi.org/10.1109/IGARSS.2018.8518512

LP DAAC - AppEEARS. (2022). Retrieved from https://lpdaac.usgs.gov/tools/appeears/

Matheson, D. S., & Dennison, P. E. (2012). Evaluating the effects of spatial resolution on hyperspectral fire detection and temperature retrieval. *Remote Sensing of Environment*, *124*, 780–792. https://doi.org/10.1016/j.rse.2012.06.026

Matson, M., & Dozier, J. (1981). Identification of subresolution high temperature sources using a thermal IR sensor. *Photogrammetric Engineering & Remote Sensing*, *47*(9), 1311–1318.

McLauchlan, K. K., Higuera, P. E., Miesel, J., Rogers, B. M., Schweitzer, J., Shuman, J. K., et al. (2020). Fire as a fundamental ecological process: Research advances and frontiers. *Journal of Ecology*, *108*(5), 2047–2069. https://doi.org/10.1111/1365-2745.13403

Miller, J. D., & Thode, A. E. (2007). Quantifying burn severity in a heterogeneous landscape with a relative version of the delta Normalized Burn Ratio (dNBR). *Remote Sensing of Environment*, *109*(1), 66–80. https://doi.org/10.1016/J.RSE.2006.12.006

Miller, R. G., Tangney, R., Enright, N. J., Fontaine, J. B., Merritt, D. J., Ooi, M. K. J., et al. (2019). Mechanisms of fire seasonality effects on plant populations. *Trends in Ecology & Evolution*, *34*(12), 1104–1117. https://doi.org/10.1016/J.TREE.2019.07.009

Morisette, J. T., Giglio, L., Csiszar, I., Justice, C. O., Giglio, L., Csiszar, I., & Justice, C. O. (2007). Validation of the MODIS active fire product over Southern Africa with ASTER data. *International Journal of Remote Sensing*, *26*(19), 4239–4264. https://doi.org/10.1080/01431160500113526

National Interagency Coordination Center. (2022). Retrieved from https://www.nifc.gov/nicc/

Nieke, J., & Rast, M. (2018). Towards the copernicus hyperspectral imaging mission for the environment (CHIME). *International Geoscience and Remote Sensing Symposium (IGARSS)*. https://doi.org/10.1109/IGARSS.2018.8518384

Pausas, J. G., & Bond, W. J. (2019). Humboldt and the reinvention of nature. *Journal of Ecology*, *107*(3), 1031–1037. https://doi.org/10.1111/1365-2745.13109

Pausas, J. G., & Keeley, J. E. (2009). A burning story: The role of fire in the history of life. *BioScience*, *59*(7), 593–601. https://doi.org/10.1525/BIO.2009.59.7.10/2/BIO.2009.59.7.10-F06

Piscini, A., & Amici, S. (2015). Fire detection from hyperspectral data using neural network approach. *Remote Sensing for Agriculture, Ecosystems, and Hydrology XVII*. https://doi.org/10.1117/12.2194911

PRISMA Documentation Area. (2020). PRISMA product specifications - issue 2.3. Retrieved from http://prisma.asi.it/missionselect/docs.php

PRISMA User Manual - Issue 1.2. (2020).

Quintano, C., Fernández-Manso, A., Calvo, L., Marcos, E., & Valbuena, L. (2015). Land surface temperature as potential indicator of burn severity in forest Mediterranean ecosystems. *International Journal of Applied Earth Observation and Geoinformation*, *36*, 1–12. https://doi.org/10.1016/J.JAG.2014.10.015

Rogers, B. M., Balch, J. K., Goetz, S. J., Lehmann, C. E. R., & Turetsky, M. (2020). Focus on changing fire regimes: Interactions with climate, ecosystems, and society. *Environmental Research Letters*, *15*(3), 030201. https://doi.org/10.1088/1748-9326/AB6D3A

Ross, A. N., Wooster, M. J., Boesch, H., & Parker, R. (2013). First satellite measurements of carbon dioxide and methane emission ratios in wildfire plumes. *Geophysical Research Letters*, *40*(15), 4098–4102. https://doi.org/10.1002/GRL.50733

Roy, D. P., Boschetti, L., & Trigg, S. N. (2006). Remote sensing of fire severity: Assessing the performance of the normalized burn ratio. *IEEE Geoscience and Remote Sensing Letters*, *3*(1), 112–116. https://doi.org/10.1109/LGRS.2005.858485

Roy, D. P., Huang, H., Boschetti, L., Giglio, L., Yan, L., Zhang, H. H., & Li, Z. (2019). Landsat-8 and Sentinel-2 burned area mapping - A combined sensor multi-temporal change detection approach. *Remote Sensing of Environment*, *231*, 111254. https://doi.org/10.1016/J.RSE.2019.111254

Sabat-Tomala, A., Raczko, E., & Zagajewski, B. (2020). Comparison of support vector machine and random forest algorithms for invasive and expansive species classification using airborne hyperspectral data. *Remote Sensing*, *12*(3), 516. https://doi.org/10.3390/RS12030516

Spiller, D., Ansalone, L., Amici, S., Piscini, A., & Mathieu, P. P. (2021). Analysis and detection of wildfires by using prisma hyperspectral imagery. *International Archives of the Photogrammetry, Remote Sensing and Spatial Information Sciences - ISPRS Archives*, *XLIII-B3-2021*. https://doi.org/10.5194/isprs-archives-XLIII-B3-2021-215-2021

Spiller, D., Ansalone, L., Carotenuto, F., & Mathieu, P. P. (2021b). Crop type mapping using prisma hyperspectral images and one-dimensional convolutional neural network. https://doi.org/10.1109/igarss47720.2021.9554175

Tobler, W. R. (1970). A computer movie simulating urban growth in the Detroit region. *Economic Geography*, *46*, 234. https://doi.org/10.2307/143141

van Leeuwen, T. T., & van der Werf, G. R. (2011). Spatial and temporal variability in the ratio of trace gases emitted from biomass burning. *Atmospheric Chemistry and Physics*, *11*(8), 3611–3629. https://doi.org/10.5194/ACP-11-3611-2011

Veraverbeke, S., Dennison, P., Gitas, I., Hulley, G., Kalashnikova, O., Katagis, T., et al. (2018). Hyperspectral remote sensing of fire: State-of-the-art and future perspectives. *Remote Sensing of Environment*, *216*, 105–121. https://doi.org/10.1016/j.rse.2018.06.020

Veraverbeke, S., Rogers, B. M., Goulden, M. L., Jandt, R. R., Miller, C. E., Wiggins, E. B., & Randerson, J. T. (2017). Lightning as a major driver of recent large fire years in North American boreal forests. *Nature Climate Change*, *7*(7), 529–534. https://doi.org/10.1038/nclimate3329

Vodacek, A., Kremens, R. L., Fordham, A. J., Vangorden, S. C., Luisi, D., Schott, J. R., & Latham, D. J. (2002). Remote optical detection of biomass burning using a potassium emission signature. *International Journal of Remote Sensing*, *23*(13), 2721–2726. https://doi.org/10.1080/01431160110109633

Waigl, C. F., Prakash, A., Stuefer, M., Verbyla, D., & Dennison, P. (2019). Fire detection and temperature retrieval using EO-1 Hyperion data over selected Alaskan boreal forest fires. *International Journal of Applied Earth Observation and Geoinformation*, *81*, 72–84. https://doi.org/10.1016/j.jag.2019.03.004

Ward, D. S., Kloster, S., Mahowald, N. M., Rogers, B. M., Randerson, J. T., & Hess, P. G. (2012). The changing radiative forcing of fires: Global model estimates for past, present and future. *Atmospheric Chemistry and Physics*, *12*(22), 10857–10886. https://doi.org/10.5194/ACP-12-10857-2012

Wooster, M. J., Roberts, G., Perry, G. L. W., & Kaufman, Y. J. (2005). Retrieval of biomass combustion rates and totals from fire radiative power observations: FRP derivation and calibration relationships between biomass consumption and fire radiative energy release. *Journal of Geophysical Research*, *110*(D24), 1–24. https://doi.org/10.1029/2005JD006318

Wooster, M. J., Roberts, G., Smith, A. M. S., Johnston, J., Freeborn, P., Amici, S., & Hudak, A. T. (2013). Thermal remote sensing of active vegetation fires and biomass burning events. In C. Kuenzer & S. Dech (Eds.), *Remote sensing and digital image processing* (pp. 347–390). Springer International Publishing. https://doi.org/10.1007/978-94-007-6639-6_18

Wooster, M. J., Roberts, G. J., Giglio, L., Roy, D., Freeborn, P., Boschetti, L., et al. (2021). Satellite remote sensing of active fires: History and current status, applications and future requirements. *Remote Sensing of Environment*, *267*, 112694. https://doi.org/10.1016/J.RSE.2021.112694

Xiang, P., Zhou, H., Li, H., Song, S., Tan, W., Song, J., & Gu, L. (2020). Hyperspectral anomaly detection by local joint subspace process and support vector machine. *International Journal of Remote Sensing*, *41*(10), 3798–3819. https://doi.org/10.1080/01431161.2019.1708504

Zanter, K. (2018). Landsat surface temperature (ST) product guide. Retrieved from https://www.usgs.gov/landsat-missions/landsat-collection-2-surface-temperature

Zheng, Z., Zeng, Y., Li, S., & Huang, W. (2016). A new burn severity index based on land surface temperature and enhanced vegetation index. *International Journal of Applied Earth Observation and Geoinformation*, *45*, 84–94. https://doi.org/10.1016/J.JAG.2015.11.002